Comparison of Experimental and Computational Simulations Results of a Pulsed Plasma Accelerator

IEPC-2005-008

Presented at the 29th International Electric Propulsion Conference, Princeton University, October 31 – November 4, 2005

T. Moeller*, D. Keefer†, R. Rhodes‡, and D. Rooney§
University of Tennessee Space Institute, Tullahoma, TN, 37388, USA

and

D. Li** and C. Merkle††
Purdue University, West Lafayette, IN 47907, USA

High power pulsed plasma thrusters (PPT) contain regions of high density plasma in close contact with regions of vacuum that challenge accurate numerical simulations using current MHD codes. A new version of the GEMS code has been developed to provide a method to accurately calculate these regions of disparate density. The GEMS code now includes a full Maxwell equation solver capable of providing both wave and diffusion solutions, and comparisons with analytical solutions and MACH2 simulations are given to demonstrate its accuracy. In addition, numerical calculations using GEMS illustrate the importance of a solution technique that handles all regimes from ideal insulator to good conductor. A MACH2 simulation of a simple Marshall gun thruster demonstrates the need for multiple regime computations in high power pulsed plasma thrusters. A laboratory Marshall gun thruster was developed to provide an array of diagnostic measurements that can be compared with the numerical simulations. The prototype thruster has been tested and a collection of photographic images, laser interferometer data, Rogowski coil data, and B-dot probe data was acquired. These measurements will provide data to compare with MACH2 and GEMS simulations.

Nomenclature

$\vec{B}$ = magnetic induction
β = pseudo-time scaling coefficient
c = speed of light
$\vec{E}$ = electric field
$\vec{J}$ = current density

* Research Associate Professor, Mechanical Engineering, Center for Laser Applications, tmoeller@utsi.edu.
† Professor Emeritus, Engineering Science, Center for Laser Applications, d_keefer@bellsouth.net.
‡ Research Scientist, Center for Laser Applications, brhodes@utsi.edu.
§ Graduate Research Assistant, Aerospace Engineering, drooney@utsi.edu.
** Research Associate Professor, Mechanical Engineering, dli@purdue.edu.
†† Reilly Professor of Engineering, Aerospace Engineering, merkle@ecn.purdue.edu.

L = characteristic length scale
t = physical time
VNN = von Neumann number = $\Delta t / \mu_0 \sigma \Delta x^2$
ε_0 = electric permittivity
φ_B = Lagrange multiplier for divergence constraint on B field
φ_E = Lagrange multiplier for divergence constraint on E field
ρ_E = electric charge density
σ = electrical conductivity
τ = pseudo time
μ_0 = magnetic permeability
Subscripts
R = reference quantity
Superscript
n = physical time step
k = pseudo-time step
* =dimensionless variable

I. Introduction

Envisioned interplanetary missions that involve on-board space nuclear power systems will provide unprecedented levels of electrical power for a variety of mission needs including planetary base support, surface exploration and operations, life support and communications. The availability of this high power capability, however, also represents a challenging opportunity for the development of new, high power electric propulsion systems whose high specific impulse and high thrust levels can shorten trip times and gross vehicle weight, thereby increasing the overall attractiveness of the mission. Highly developed conventional EP thrusters such as ion engines, Hall thrusters and arcjets are well suited for lower power applications but have not been scaled to the power levels anticipated with fission-based space nuclear electric power systems. These smaller thrusters utilize electrostatic and thermal processes to provide thrust from a plasma propellant. Electromagnetic acceleration of plasmas for propulsion has long been seen as a means of providing efficient high specific impulse propulsion systems, however, development of this class of accelerators has languished because they are efficient only at power levels that heretofore have been unavailable in space.

Two distinct types of electromagnetic thrusters have been suggested for the high power arena: magnetoplasmadynamic (MPD) thrusters, which are steady flow devices, and Pulsed Plasma Accelerators (PPA) that are variants of the Marshall Gun. These devices operate in different magnetic interaction regimes. The MPD operates at relatively small magnetic Reynolds number (R_m) while the PPA operates at large R_m. Pulsed systems are particularly of interest because they can be operated over a wide range of available power by varying the pulse duty cycle to retain efficient high-power operation while controlling average power.

In the present paper we present initial results from a companion experimental/computational effort aimed at addressing the physical behavior and performance characteristics of high power pulsed plasma thrusters for possible applications in nuclear electric propulsion systems. The experimental portion of the program utilizes a laboratory prototype PPA that is designed to provide both detailed experimental diagnostics of PPA operation and accurate diagnostic data for validation of the companion computational simulations. The computational effort involves detailed simulations with two codes: the widely accepted MACH2 plasma dynamics code which is based on the MHD approximation and a somewhat simplified fluid dynamics capability, and a new in-house Maxwell solver known as GEMS that incorporates complete fluid dynamics capabilities and allows either MHD or full Maxwell solutions. One important role of the MACH2 code is to serve as a standard against which simulations from the newer GEMS code can be verified and to provide a historical link to the wide array of MACH2 calculations which have previously been done in our laboratory and elsewhere. Both MACH2 and GEMS are used for data interpretation and guidance to the experiments with the intention being to transfer more and more of this role to GEMS as its capabilities and consistency with MACH2 are verified. In addition, GEMS is being used to understand physics issues in areas where the MHD approximation is invalid and MACH2 cannot be used directly.

The organization of the paper is a follows. Section II discusses the PPA configuration of interest and presents the details of the experimental laboratory prototype and some initial representative experimental data. Preliminary simulations of PPA operation from the MACH2 code are also presented in this section. In section III we present the electromagnetic implementation that is being used in GEMS with emphasis on a hyperbolic solution technique that is applicable to either the MHD equations of the complete Maxwell set. Section IV then presents the results of some

simple representative test problems that have been obtained from GEMS along with validation against closed form analytical solutions and companion MACH2 calculations. Section V summarizes our findings.

II. Experiment

To provide validation data for computer simulations, we are developing a laboratory prototype pulsed plasma accelerator with an emphasis on providing accurate diagnostics as opposed to optimized thruster performance. MACH2 simulations were utilized to guide the design of this prototype. This thruster has been successfully fired, and ongoing testing is providing data with which planned simulations can be compared. The experimental setup and representative data from early testing are presented in this section.

A. Experimental Setup

The thruster consists of a cylindrical center body 2-inches in diameter inside of a coaxial 4-inch diameter tube (Fig. 1). This outer tube is divided into a 2-inch upstream section and a 5-inch downstream section by a quartz insulating ring. The ring has sputtered metal strips connecting the two sections of the tube which, when vaporized by an ignition power supply, provides the plasma propellant that triggers and then is driven by the main power supply. The main power source, a 17.5 μF 40 kV capacitor charged with a 30 kV power supply, provides a maximum energy storage of almost 8 kJ with a calculated discharge time of 10 μs and an average power of nearly 800 megawatts[1].

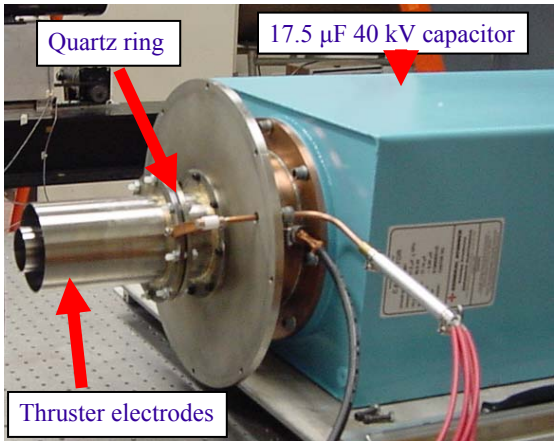

Figure 1. Photograph of prototype pulsed

Early system firing resulted in a fuse plasma that was not azimuthally uniform. To promote azimuthal symmetry, we placed axial slots in the outer electrode between the quartz fuse ring and the downstream trigger capacitor connection (Fig. 2). These slots create an array of parallel inductances between the fuse and the trigger power supply that act as an inductive divider to drive the current flowing through the electrode towards uniformity. To further promote the generation of a uniform discharge, the inner electrode was modified to include 1/8" wide slots that run almost the entire length of the electrode. This creates an inductive divider through which the main capacitor current must pass immediately following current initiation, rather than being delayed until the current sheet reaches the slotted section of the outer electrode downstream of the quartz fuse ring.

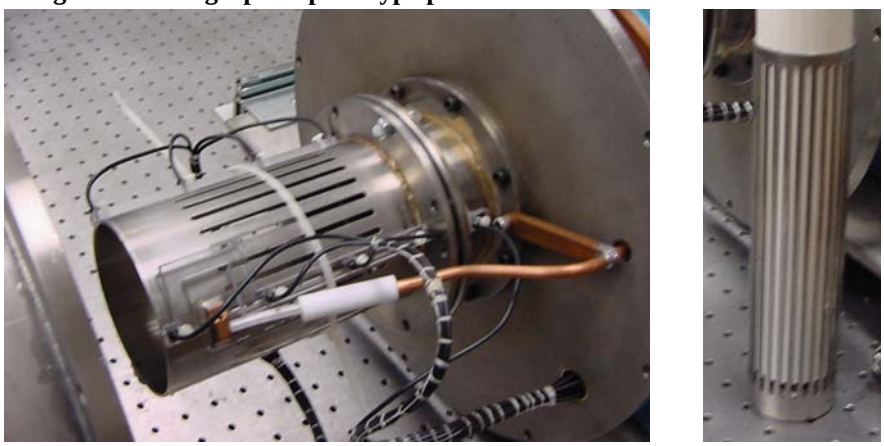

Figure 2. Photograph showing details of slotted outer (left) and and inner (right) electrodes.

The thruster is installed in a vacuum chamber fabricated from stainless steel tubing and plate (Fig. 3). The plasma discharges through a section of vacuum chamber with flat quartz windows that are used for interferometric, photographic, and spectroscopic measurements. An Imacon high speed camera is positioned to take photographs at up to 20 million frames per second. A single beam, heterodyne laser interferometer has been installed to obtain line-of-sight electron number density data downstream of the exit plane. Rogowski coils have been installed to monitor the current in the trigger and main capacitor circuits. Thirteen B-dot probes (see the left photograph in Fig. 2) have been installed on the outer electrode and are being utilized to help characterize the development of the current sheet inside of the thruster. The B-dot probes are connected to, 20 MHz data acquisition channels.

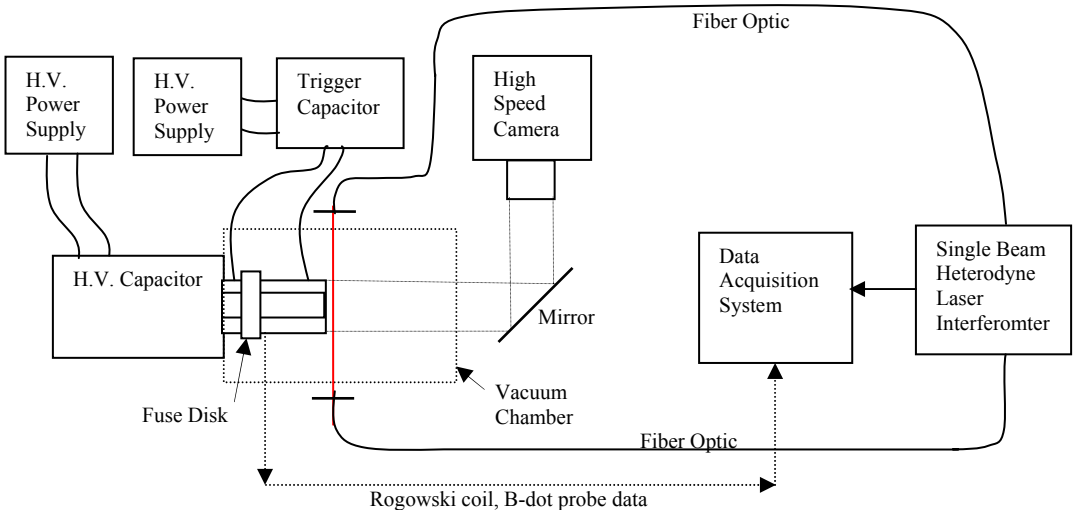

Figure 3. Schematic of Experimental Setup.

B. Preliminary Thruster Data

Example outputs from the diagnostics were collected in tests with the main high voltage capacitor charged to 20 kV. The trigger current and main capacitor current as a function of time for this case are shown in Figs. 4 and 5, respectively. A high-speed photograph of the end-on view of the discharge is shown in Figure 6. The frames in this figure were taken at a rate of 1 MHz with time progressing from bottom-to-top and from left-to-right. The peak current in the main capacitor is approximately 160,000 *A* and that in the trigger circuit is approximately 16,000 *A*. Representative path-integrated line-of-sight electron number densities calculated from data taken from the heterodyne laser interferometer[2] are shown in Fig 7.

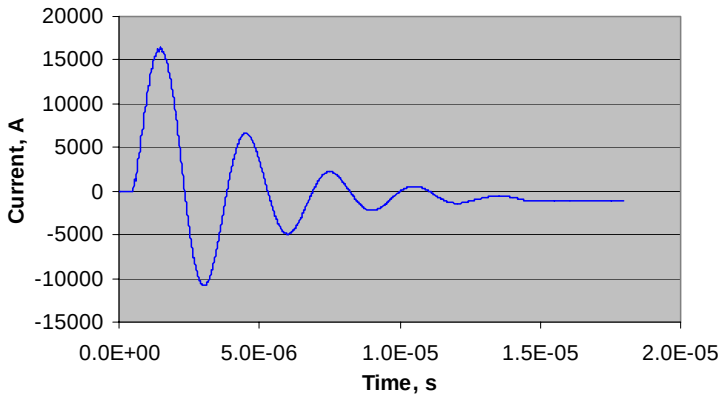

Figure 4. Time resolved trigger circuit current measured using a Rogowski coil.

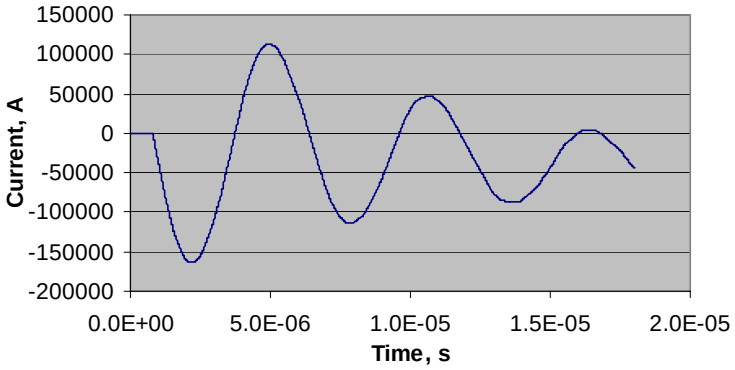

Figure 5. Time resolved current in the thruster circuit measured using a Rogowski coil.

Representative integrated B-dot probe data are shown in Fig. 8. Tracking the peaks in the probe data as a function of time along with the known probe positions can be utilized to estimate an average velocity of various peaks in the current sheet as it propagates in the thruster. The first peak is the best choice because it is the strongest and easiest to identify. Although analysis of the B-dot data is just commencing, preliminary results indicate that the average velocity of the current sheets ranges from roughly 480 km/s for the first current peak to roughly 59 km/s for the forth current peak. The decrease in

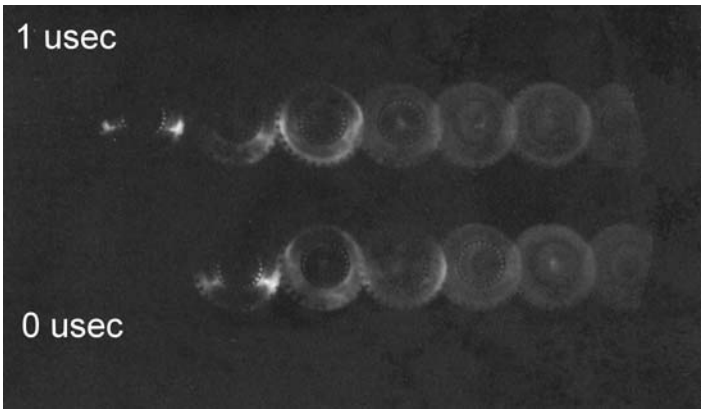

Figure 6. High-speed photograph of discharge (end-on view).

current sheet velocity with cycle peak number is attributed to that fact that a larger percentage of propellant mass is ejected from the thruster with each current cycle. This trend is predicted by preliminary MACH2 simulations that indicate an initial, low-mass puff of propellant exits the thruster at approximately 100 km/s, but the majority of the propellant mass exits the thruster at much lower velocities. Detailed comparisons between simulations and experimental data are not available for this paper but will be given in future publications.

C. Preliminary MACH2 Thruster Simulation Results

MACH2 is a time dependent magnetohydrodynamics (MHD) computer code that can be run in the axisymmetric mode[3]. When modeling with MACH2, there exists a class of problems where a conductor, usually a plasma, bridges the walls downstream of the point where the circuit is attached and an insulating gas or 'vacuum' fills the intervening space. In the corresponding physical device the magnetic field propagates across the vacuum as a wave. MACH2 does not model electromagnetic propagation by waves, and some other mechanism is necessary to allow the current to move from the point of circuit attachment. The transport mechanisms for a magnetic field included in the MACH2 MHD code are convection, diffusion, and the Hall Effect. All of these have been used to transport magnetic field across the vacuum with differing degrees of success.

During the past several years we at UTSI have been experimenting with and modeling pulsed plasma thrusters and, more recently, a pulsed plasma accelerator (Fig. 9). In the PPA, the plasma is formed from an exploding foil which, after a short delay, bridges the annular gap discharging the main capacitor. When modeling this device we have chosen to use diffusion to propagate the magnetic field from the capacitor connections to the plasma armature. To implement this we employ an ideal fluid we call 'ether' named after the fluid which, before the development of wave theory, was believed to occupy all

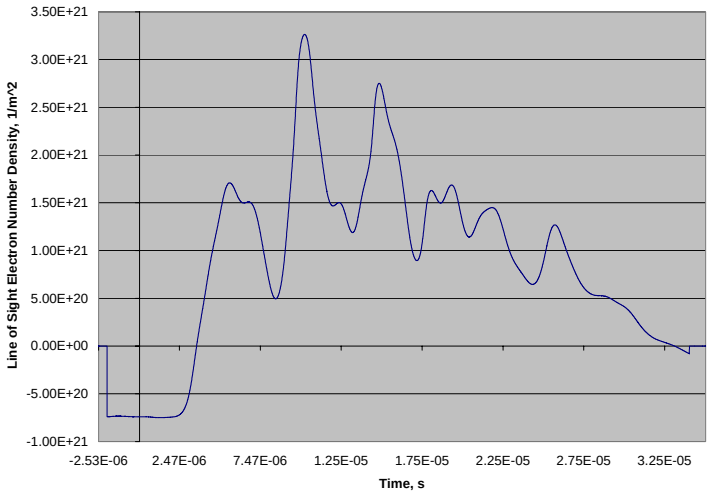

Figure 7. Line-of-sight electron number density determined from the heterodyne laser interferometer.

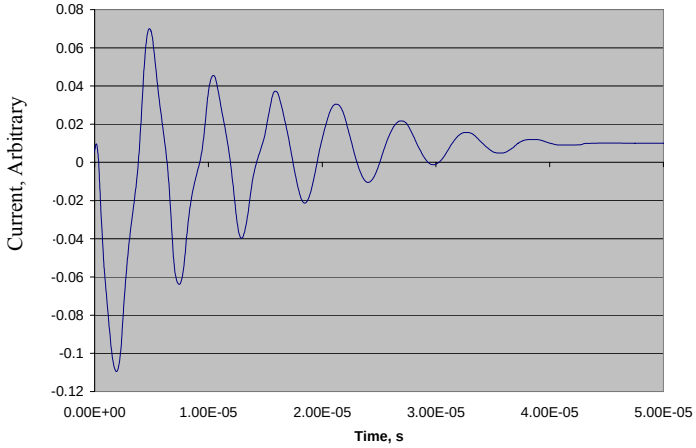

Figure 8. Sample integrated data from a B-dot probe located between the main capacitor and the fuse disk.

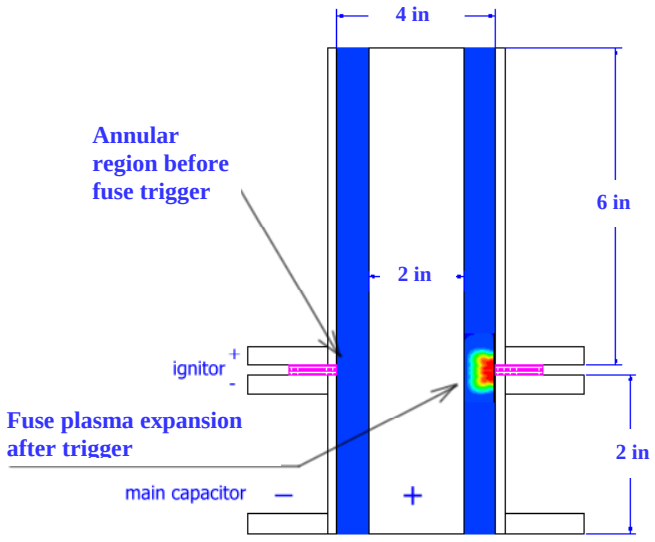

Figure 9. Schematic of laboratory prototype pulsed plasma thruster.

space and provided the medium to propagate light. Our ether has a low molecular weight to minimize its effect on the total mass of propellant, a large constant resistivity to promote rapid diffusion, suppressed ohmic heating to avoid temperature runaway, and a high viscosity to damp any vortices that might form and trap magnetic fields.

Thrusters and opening switches where wave propagation may occur usually operate on microsecond time scales rather than the nanosecond or picosecond scales where electromagnetic waves propagate. The question usually addressed is how does the plasma move under the influence of the magnetic and fluid mechanical pressures, rather than the detailed distribution of the magnetic field. A calculation was made with MACH2 using a sinusoidal current input with a one microsecond rise time across the annular gap between a 50 mm and a 100 mm tube. The tubes were shorted 50 mm from the inlet. Figure 10 shows rB_θ in *A* as a function of time at the short and at the current connection. The von Neumann number (VNN) for this run is approximately 10^5, at least 3 orders of magnitude too large to give an accurate solution to the diffusion equation. The time for an electromagnetic wave to travel 50mm in vacuum is 166 picoseconds, negligible on this time scale. So the short would feel the inlet condition almost instantaneously if light speed propagation were available in the model. The magnetic field at the short initially lags, but even with the errors from a much too large a VNN, after 300 nanoseconds there is negligible difference in the magnetic field at the short between diffusion and light speed transmission. A computation of the thruster impulse at 1 microsecond shows about 0.5% difference between the two assumptions. It would be possible to run the initial phase at a smaller VNN and then increase the time step when the field stalls at the plasma armature. The problem occurs when the magnetic field breaks through the plasma and large magnetic fields try to move through regions of very low density. At this point the VNN increases at various times and places in the flow unless the time step is reduced, possibly to a point where the run cannot be completed. It may be necessary to run with large VNN's to complete thruster and opening switch calculations in an acceptable amount of time. With GEMS we now have a tool where such regions may be examined in detail to evaluate the effects of cruder approximations.

The question of solving the diffusion equation with an excessive VNN was also examined by calculating the propagation of a magnetic field from a step function input of 400,000 *A* into a short 50 mm from the inlet (Fig. 11). The VNN was controlled by setting the maximum time step. The speed of propagation is reduced at larger time steps and at a VNN of 1000 the errors in the solution become significant in this problem. Since this method is at best a crude approximation of wave propagation, a computational method is needed that can incorporate both wave and diffusion

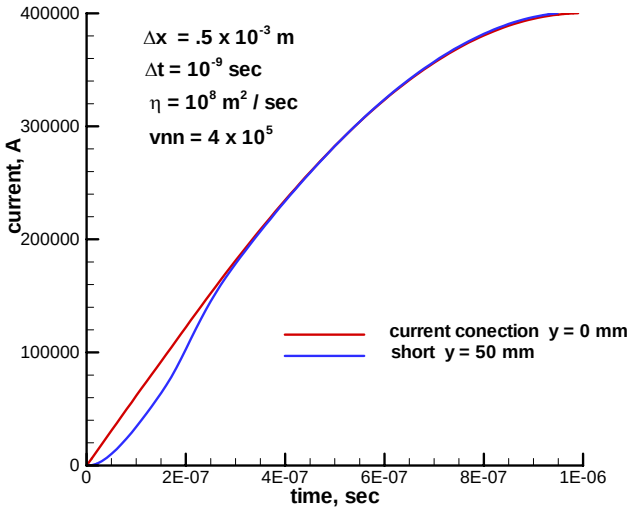

Figure 10. Current delay across a 50 mm insulating gap.

propagation of magnetic fields.

An example of one PPA simulation that utilizes Teflon® as a propellant is presented below to demonstrate the time-evolution of the magnetic field and propellant mass distributions in such a device. A calculation using MACH2 was used to simulate a thruster with a Marshall gun[4] configuration with an annular gap of 25mm confined by 3mm thick walls. In this simulation, the initial condition employed an ionized Teflon® plasma (with a density of 0.056 kg/m^3) filling the annulus between 50 and 55mm axially. The gun is driven by a 400,000 *A* sinusoidal current pulse with a 1.3 μsec rise time. The circuit is connected between the coaxial electrodes at the upstream end of the thruster (bottom of Fig 12). The magnetic field is shown as $2\pi rB_\theta/\mu_o$ in Fig. 12, and the region of high Teflon density is shown by two contour lines corresponding to 0.07 kg/m^3 and 0.0005 kg/m^3. At 1 μsec after current initiation the plasma has been slightly compressed and distorted from its original position, and the magnetic field is essentially confined by the plasma. At 1.25 μsec there is significant distortion of the plasma near the center-body where the Lorentz force is largest, since both the magnetic inductance, B, and the current density, J, decrease with radius. The magnetic field is still essentially confined by the plasma. At 1.5 μsec the magnetic field has broken through the plasma augmented by radial components of the Lorentz force that push the plasma toward the walls. At this point the magnetic field is again propagating into a vacuum and wave-like propagation must be included or simulated by another mechanism. Accurate modeling of these regions of widely varying plasma density will provide a tool which will allow a better understanding of the physical processes in a PPA. The electro-magnetic version of the GEMS code is being developed for this purpose.

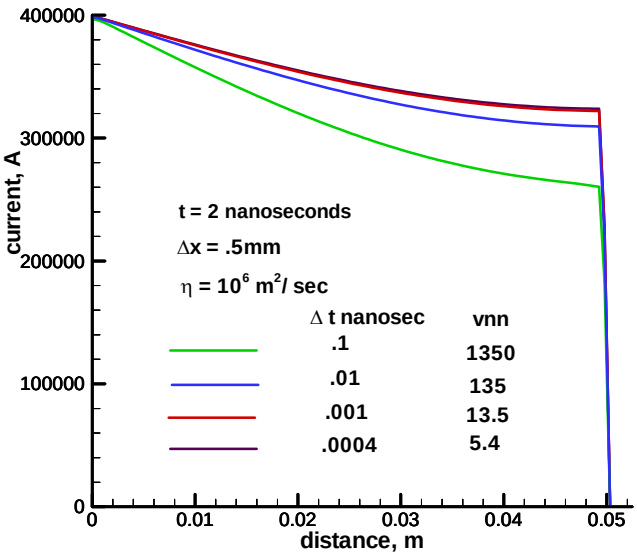

Figure 11. Effect of Δt on solution accuracy.

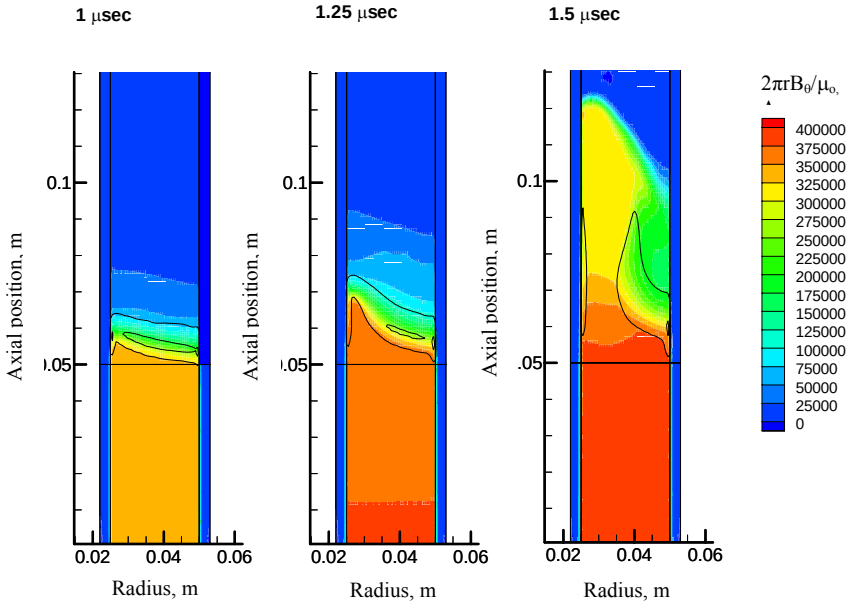

Figure 12. Magnetic field and Plasma in a coaxial PPA.

III. Formulation of the Combined Parabolic/Hyperbolic Problem

Maxwell's equations for a linear, isotropic medium are,

$$\frac{1}{c^2}\frac{\partial \vec{E}}{\partial t} - \nabla \times \vec{B} = -\mu_0 \vec{J} \tag{1}$$

$$\frac{\partial \vec{B}}{\partial t} + \nabla \times \vec{E} = 0 \tag{2}$$

$$\nabla \bullet \vec{B} = 0 \tag{3}$$

$$\nabla \bullet \vec{E} = \rho_e / \varepsilon_0 \tag{4}$$

where $\vec{E}$ is the electric field; $\vec{B}$ is the magnetic induction and $\vec{J}$ is the current density. The quantities, ε_0 and μ_0, are the electric permittivity and the magnetic permeability of free space, respectively; while c, is the speed of light; and ρ_e is the electric charge density. To express the current density in terms of the field quantities, we introduce a generalized Ohm's law as

$$\vec{E} = -\vec{V} \times \vec{B} + \frac{1}{\sigma}\vec{J} + \frac{1}{ne}\vec{J} \times \vec{B} \tag{5}$$

where $\vec{V}$ is the plasma particle velocity, σ is the electrical conductivity, *n* is the electron number density, and *e* is the charge on an electron. Ohm's law can be inverted to express the current density in terms of the electric and magnetic fields by defining a general electrical conductivity tensor, Λ, as,

$$\Lambda = \frac{1}{\sigma}\begin{pmatrix} 1 & \frac{\sigma}{ne}B_z & -\frac{\sigma}{ne}B_y \\ -\frac{\sigma}{ne}B_z & 1 & \frac{\sigma}{ne}B_x \\ \frac{\sigma}{ne}B_y & -\frac{\sigma}{ne}B_x & 1 \end{pmatrix} \tag{6}$$

to give,

$$\vec{J} = \Lambda^{-1}(\vec{E} + \vec{V} \times \vec{B}) \tag{7}$$

Combining Eqs. 1 and 7 gives,

$$\frac{1}{c^2}\frac{\partial \vec{E}}{\partial t} - \nabla \times \vec{B} = -\mu_0 \Lambda^{-1}(\vec{E} + \vec{V} \times \vec{B}) \tag{8}$$

The results in the present paper are based on the simpler form $\vec{J} = \sigma \vec{E}$ in which the tensor, Λ^{-1}, reduces to the scalar, σ, and the velocity is taken as zero. Although this simpler form is used to demonstrate the approach, all conclusions can be interpreted in term of this more general formulation.

There are three distinct temporal regimes in which solutions of Maxwell's equations are of interest: (i) a quasi-steady regime where $\partial \vec{E}/\partial t = \partial \vec{B}/\partial t = 0$ and the partial differential equations reduce to the statements that both the divergence and curl of the vector $\vec{B}$ vanish while the curl of $\vec{E}$ vanishes, but its divergence depends on the space charge; (ii) a parabolic, MHD regime where $\left(1/c^2\right)\partial \vec{E}/\partial t = 0$, but $\partial \vec{B}/\partial t \neq 0$ so that Maxwell's equations reduce to the magnetic diffusion equation; and (iii) a hyperbolic, Maxwell regime where both $\partial \vec{E}/\partial t$ and $\partial \vec{B}/\partial t$ are non-zero and electromagnetic effects travel by wave-like processes. These three regimes can be illustrated by combining the above set of equations into a single equation for the magnetic field. Taking the curl of the first equation and combining with the temporal derivative of the second while using the divergence constraint on the magnetic field gives the convected wave equation:

$$\frac{1}{c^2}\frac{\partial^2 \vec{B}}{\partial t^2} + \mu_0 \sigma \frac{\partial \vec{B}}{\partial t} = \nabla^2 \vec{B} \tag{9}$$

The quasi-steady regime occurs when both the first and second temporal derivatives of B are negligibly small. The diffusion regime corresponds to the case where the source term, $\mu_0\sigma$, is large and the second-order temporal derivative can be omitted. Physically, this condition corresponds to applications in which the displacement current is negligible in comparison with the physical current, $\varepsilon_0 \partial \vec{E} / \partial t << \vec{J}$. When the source term is small, the displacement current must balance the curl of the magnetic field, and the equation takes the classical form of the wave equation. Succinctly, for small values of physical current where the displacement current is significant, disturbances travel as waves, but for large values of physical current and negligible displacement current, they propagate by diffusion as the above equation indicates.

Although closed form solutions to these equations can be found for isolated cases in all three regimes, complex domains and general boundary configurations require numerical solutions. Our goal in the present paper is to present a single method that will allow solutions in all three regimes. Such a method is convenient for general applications, but is mandatory for propulsion applications such as those discussed in the Sections above where diffusion and wave-like regimes occur in different portions of the same problem.

Before looking at the numerical solution of the general problem, we note that distinct numerical methods are widely used for both the diffusion and wave-like regimes. In the diffusion regime, which is generally associated with MHD problems, solutions are generally obtained by combining Faraday's law and Ampere's law to give the second-order magnetic diffusion equation[5, 6]. A key issue with such methods is identifying a technique for enforcing the divergence constraint because discrete forms of the *div* and *curl* operators do not generally satisfy the vector identity that *div curl* = 0. One method for enforcing this vector identity has been suggested by Powell[7], and adapted by various others including ourselves[8-10]. Staggered grid methods represent an exception to this discrete inconsistency and can be used without a special divergence constraint. Wave equation solutions in the Maxwell regime are also widely used in both the time and frequency domains. Numerical methods in the time domain are generally based upon the first order equations as given above, and are restricted to problems in which the physical current is small.

A. Incorporating Pseudo-Time

The magnetic diffusion equation constitutes an efficient description of problems for which the displacement current is negligible, but it fails when the displacement current becomes significant, since this term has been dropped altogether. Direct, time-marching solutions of the original first-order form of the equations appears attractive for problems in which both physical current and displacement current are significant, but these methods fail when the displacement current is small because the temporal derivative of the electric field disappears and leaves no update method for the E-field. Time-marching methods also encounter difficulties in enforcing the two divergence constraints which again have no temporal derivatives. To circumvent these difficulties, we use Lagrange multipliers to add two potential-like functions to the divergence constraints[11] to bring the equation set to an eight-by-eight system and fashion an iterative method for this coupled system in terms of a pseudo-time which contains non-zero pseudo-time derivatives for all equations and therefore allows marching in pseudo-time. The pseudo-time corresponds to iterating to the proper transient condition at each physical time step. We denote the pseudo time by the symbol, τ, to distinguish it from the physical time, t.

The modified Maxwell's equations with the Lagrange multipliers, φ_B and φ_E, included and with pseudo-time derivatives added to all equations become:

$$\frac{1}{\beta c^2}\frac{\partial \vec{E}}{\partial \tau} + \frac{\partial \vec{E}}{\partial t} - \nabla \times \vec{B} + \nabla \varphi_E = -\mu_0 \sigma \vec{E} \tag{10}$$

$$\frac{\partial \vec{B}}{\partial \tau} + \frac{\partial \vec{B}}{\partial t} + \nabla \times \vec{E} + \nabla \varphi_B = 0 \tag{11}$$

$$\frac{1}{\beta c^2}\frac{\partial \varphi_B}{\partial \tau} + \nabla \bullet \vec{B} = 0 \tag{12}$$

$$\frac{\partial \varphi_E}{\partial \tau} + \nabla \bullet \vec{E} = \frac{1}{\varepsilon_0}\rho \tag{13}$$

The pseudo-time enables us to use a common hyperbolic method to provide solutions in all three regimes. In the limit as the pseudo-time goes to infinity, the two potential-like functions go to zero and the divergence constraints are recovered for either steady or transient conditions. Efficient solution of the pseudo-time equations, however, requires the definition of a scaling coefficient, β, to ensure that the pseudo-time derivatives match the dominant terms in the equation in each of the three regimes. This choice can be made by non-dimensionalizing the terms in the equations in such a manner that they are balanced for each regime, and selecting β so that the pseudo-time derivatives are balanced with the physical terms.

B. Scaling the Pseudo-Time Equations

We non-dimensionalize the equations by defining reference quantities denoted by subscript *R*, and dimensionless variables denoted by a superscript asterisk. The non-dimensional pseudo-time equations are:

$$\frac{B_R}{\tau_R}\frac{\partial \vec{B}^*}{\partial \tau^*} + \frac{B_R}{t_R}\frac{\partial \vec{B}^*}{\partial t^*} + \frac{E_R}{L}\nabla \times \vec{E}^* + \frac{\varphi_{BR}}{L}\nabla^* \varphi_B^* = 0 \tag{14}$$

$$\frac{E_R}{\beta c^2 \tau_R}\frac{\partial \vec{E}^*}{\partial \tau^*} + \frac{E_R}{t_R}\frac{1}{c^2}\frac{\partial \vec{E}^*}{\partial t^*} - \frac{B_R}{L}\nabla^* \times \vec{B}^* + \frac{\varphi_{ER}}{L}\nabla \varphi_E^* = -\mu_0 \sigma E_R \vec{E}^* \tag{15}$$

$$\frac{\varphi_{BR}}{\beta c^2 \tau_R}\frac{\partial \varphi_B^*}{\partial \tau^*} + \frac{B_R}{L}\nabla^* \bullet \vec{B}^* = 0 \tag{16}$$

$$\frac{\varphi_{ER}}{\tau_R}\frac{\partial \varphi_E^*}{\partial \tau^*} + \frac{E_R}{L}\nabla^* \bullet \vec{E}^* = \frac{1}{\varepsilon_0}\rho \tag{17}$$

For the quasi-steady limit, we choose the reference *B*-field as $B_R \equiv \mu_0 \sigma L E_R$ so that the *curl B* term balances the physical current and the reference potential $\varphi_{ER} \equiv B_R$ to balance the reference *B*-field. Ampere's law then becomes,

$$\frac{1}{\mu_0 \sigma c^2 \beta}\frac{1}{\tau_R}\frac{\partial \vec{E}}{\partial \tau} - \nabla \times \vec{B} + \nabla \varphi_E = -\vec{E} \tag{18}$$

where we have dropped the displacement current since we are interested in the quasi-steady condition.

Applying this scaling to the remaining three equations and defining $\varphi_{BR} \equiv E_R$ gives:

$$\frac{\mu_0 \sigma L^2}{\tau_R}\frac{\partial \vec{B}}{\partial \tau} + \nabla \times \vec{E} + \nabla \varphi_B = 0 \tag{19}$$

$$\frac{1}{\mu_0 \sigma c^2 \beta}\frac{1}{\tau_R}\frac{\partial \varphi_B}{\partial \tau} + \nabla \bullet \vec{B} = 0 \tag{20}$$

$$\frac{\mu_0 \sigma L^2}{\tau_R}\frac{\partial \varphi_E}{\partial \tau} + \nabla \bullet \vec{E} = \frac{1}{\varepsilon_0}\rho \frac{L}{E_R} \tag{21}$$

To ensure efficient convergence, the pseudo-time derivatives must balance the dominant physical terms. Accordingly, for the quasi-steady limit, we define, $\tau_R = \mu_0 \sigma L^2$ and $\beta = (\mu_0 \sigma c L)^{-2}$. This equation is properly ordered so long as $\mu_0 \sigma c^2 t_R >> 1$. That is to say, it is pertinent for large characteristic physical times.

For the diffusion equation limit we balance the *curl E* term with the *B-dot* term in Faraday's law by choosing the reference *B*-field as $B_R \equiv E_R t_R / L$. Faraday's law then becomes,

$$\frac{t_R}{\tau_R}\frac{\partial \vec{B}}{\partial \tau} + \frac{\partial \vec{B}}{\partial t} + \nabla \times \vec{E} + \nabla \varphi_B = 0 \tag{22}$$

Using this reference condition in Ampere's law then gives,

$$\frac{1}{\beta}\left(\frac{L}{ct_R}\right)^2 \frac{t_R}{\tau_R}\frac{\partial \vec{E}}{\partial \tau} - \nabla \times \vec{B} + \nabla \varphi_E = -\frac{\mu_0 \sigma L^2}{t_R}\vec{E} \tag{23}$$

where we have again dropped the displacement current.

To order this equation properly we note that time-accurate solutions of a diffusion equation require that the physical time step be chosen such that the von Neumann number, $VNN = \Delta t / \mu_0 \sigma \Delta x^2$ be of order one. Accordingly, we choose the physical characteristic time as $t_R = \Delta t$ and the characteristic length scale as the grid size, $L = \Delta x$, so that $t_R = \Delta t = VNN \mu_0 \sigma \Delta x^2$. Balancing the remaining terms in the equation then gives, $\tau_R = \Delta t$ and $\beta = \left(VNN \mu_0 \sigma c \Delta x\right)^{-2}$. The scaling of the two potential-like functions is the same as in the quasi-steady case.

The limit in which the displacement current is significant proceeds in like fashion. For this condition, the reference *B*- and *E*-fields are related as, $E_R = B_R t_R c^2 / L$. Here we choose the physical characteristic time from the CFL value recognizing that the characteristic velocity is the speed of light when the full Maxwell solution is used. Therefore, we have, $t_R = \Delta t = CFL \Delta x / c$, where *CFL* is of order one. The scaling then gives $\tau_R = L / CFLc$ and $\beta = 1$. The results of the scaling procedure are given in Table I for all three regimes.

In employing the method, the full Maxwell equations (including the temporal derivatives of both $\vec{B}$ and $\vec{E}$) are retained at all points throughout the domain. The value of β is then defined for every cell within the computational domain according to local conditions. The hyperbolic pseudo-time iterative method is then used to converge the solution at each physical time step. Thus, for example, if the displacement current is significant over a portion of the computational domain it is evaluated throughout the domain, but has no impact in regions where it is small. For problems where the displacement is everywhere small, the user has a choice of omitting or including the displacement current in the entire domain. If it is truly negligible, the solutions will be essentially identical.

Table I
Values of Scaling Factor, β

Limit	β
Quasi-Steady Limit	$\beta = \left(\frac{1}{\mu_0 \sigma c L}\right)^2$
MHD Limit	$\beta = \left(\frac{1}{VNN}\frac{1}{\mu_0 \sigma c \Delta x}\right)^2$
Maxwell Limit	$\beta = 1$

C. Numerical Solution of the Equations

The introduction of the pseudo-time derivatives allows us to iterate at each physical time step to ensure that the proper solution at each time step is obtained after a series of iterations. Because the pseudo-time is formulated in a hyperbolic form with a complete independent variable vector, we can use a hyperbolic method to perform the iterations at each time step even if the equations are parabolic in physical time. Although time-accurate calculations traditionally require a method that is second-order accurate, we here symbolically use first-order Euler implicit differencing in physical time to simplify the notation. For the physical time, we use a superscript n to indicate the

previous (known) time level and a tilde to denote the new (unknown) time level such that a representative time derivative becomes:

$$\frac{\partial \widetilde{E}}{\partial t} = \frac{\widetilde{E} - E^n}{\Delta t} \tag{24}$$

After differencing in physical time, the equations become:

$$\frac{1}{\beta c^2}\frac{\partial \widetilde{E}}{\partial \tau} + \frac{1}{c^2}\frac{\widetilde{E} - E^n}{\Delta t} - \nabla \times \widetilde{B} + \nabla \widetilde{\varphi}_E = -\mu_0 \sigma \vec{E} \tag{25}$$

$$\frac{\partial \vec{B}}{\partial \tau} + \frac{\widetilde{B} - B^n}{\Delta t} + \nabla \times \widetilde{E} + \nabla \widetilde{\varphi}_B = 0 \tag{26}$$

$$\frac{1}{\beta c^2}\frac{\partial \widetilde{\varphi}_B}{\partial \tau} + \nabla \bullet \widetilde{B} = 0 \tag{27}$$

$$\frac{\partial \widetilde{\varphi}_E}{\partial \tau} + \nabla \bullet \widetilde{E} = \frac{1}{\varepsilon_0}\rho_e \tag{28}$$

These equations are now discretized in pseudo time using the superscripts k and k+1 to give

$$\frac{\widetilde{E}^{k+1} - \widetilde{E}^k}{\beta c^2 \Delta \tau} + \frac{\widetilde{E}^{k+1} - \widetilde{E}^k + \widetilde{E}^k - E^n}{c^2 \Delta t} - \nabla \times \widetilde{B}^{k+1} + \nabla \widetilde{\varphi}_E^{k+1} = -\mu_0 \sigma \vec{E}^{k+1} \tag{29}$$

$$\frac{\vec{B}^{k+1} - \vec{B}^k}{\Delta \tau} + \frac{\widetilde{B}^{k+1} - \widetilde{B}^k + \widetilde{B}^k - B^n}{\Delta t} + \nabla \times \widetilde{E}^{k+1} + \nabla \widetilde{\varphi}_B^{k+1} = 0 \tag{30}$$

$$\frac{\widetilde{\varphi}_B^{k+1} - \widetilde{\varphi}_B^k}{\beta c^2 \Delta \tau} + \nabla \bullet \widetilde{B}^{k+1} = 0 \tag{31}$$

$$\frac{\widetilde{\varphi}_E^{k+1} - \widetilde{\varphi}_E^k}{\Delta \tau} + \nabla \bullet \widetilde{E}^{k+1} = \frac{1}{\varepsilon_0}\rho_e^{k+1} \tag{32}$$

The spatial derivatives are discretized by a second-order accurate upwind, finite-volume process, and solved by an approximate Riemann solver[12, 13]. Representative results from this method are given in the following section.

IV. Simulation Results

To demonstrate the capability of the GEMS code for the full Maxwell equations, we discuss numerical experiments where the Maxwell solver is applied in different situations. First, the diffusion of a magnetic field through a finite conductor in response to a step change in the magnetic field at the boundary is presented and compared with a corresponding analytical solution to demonstrate that the hyperbolic implementation produces accurate results for the diffusion problem. Following, we contrast the approximate diffusion solution to a complete Maxwell solution for cases where the diffusivity is small enough that wave processes becomes important. We then look at the magnetic field propagation through a domain composed of a vacuum region enclosed by finite conducting walls. As an approximation we fill the vacuum region with 'ether' having a finite conductivity and compare numerical solutions for the rate of diffusion of magnetic field through the ether as obtained with the MACH2 MHD code, which solves the magnetic diffusion equation, and the present GEMS formulation which can solve either the full Maxwell equations or the diffusion approximation. The results show excellent agreement between the present code and the MACH code, while also showing the dramatic differences in the manner in which magnetic fields propagate by wave processes sustained by displacement current, and in diffusion processes sustained by physical current.

A. One-Dimensional Diffusion Problem

As an initial verification of the computational method, we consider the temporal evolution of the electric and magnetic fields in a one-dimensional, semi-infinite domain, $0 \le x < \infty$. To enable comparison with an analytical solution, the displacement current term, $\left(1/c^2\right)\partial\vec{E}/\partial t$, is neglected so that the magnetic diffusion equation applies. The corresponding electric field is then given by the curl of the magnetic field, $\vec{E} = \left(\nabla \times \vec{B}\right)/\mu_0\sigma$. As the initial condition, the electric and magnetic fields are set to zero throughout the domain. At time zero, the boundary condition on the axial component of the magnetic field at $x = 0$, steps from $B_z = 0$ to $B_z = B_0$ and remains constant for all time. The other two magnetic field components at $x = 0$, and all three components as $x \to \infty$ remain unchanged. Under these conditions the only non-zero components of the solution are the z-axial magnetic field, B_z, and the transverse electric field, E_y, and the magnetic diffusion equation reduces to a one-dimensional equation that possesses the similarity solution:

$$B_z = B_0\left\{1 - erf\left(\frac{x}{2}\sqrt{\frac{\mu_0\sigma}{t}}\right)\right\} \qquad B_x = B_y = 0 \tag{33}$$

$$E_y = \frac{1}{\mu_0\sigma}\frac{\partial B_x}{\partial x} = \sqrt{\frac{1}{\pi\mu_0\sigma t}}\exp\left(\frac{x}{2}\sqrt{\frac{\mu_0\sigma}{t}}\right) \qquad E_x = Ez = 0 \tag{34}$$

To provide a numerical solution for comparison with this analytical result we consider a two-dimensional solution of the first-order Maxwell equations with the displacement current omitted,

$$\frac{1}{\beta c^2}\frac{\partial\vec{E}}{\partial\tau} - \nabla\times\vec{B} = -\mu_0\sigma\vec{E} \tag{35}$$

$$\frac{\partial\vec{B}}{\partial\tau} + \frac{\partial\vec{B}}{\partial t} + \nabla\times\vec{E} = 0 \tag{36}$$

The divergence constraints are automatically satisfied in the one-dimensional limit so the Lagrange multipliers are omitted. Numerical solutions for this first-order analog of the diffusion equation are obtained on a two-dimensional, uniform grid of size 176x105 for the finite domain $0 \le x \le 1$, $0 \le y \le 0.3$ with boundary conditions $B_z = B_0$, $\partial E_y/\partial x = 0$ on x= 0, along with a zero slope condition, $\partial\vec{B}/\partial n = \partial\vec{E}/\partial n = 0$, on the remaining three sides. Applying a zero-slope condition at a finite location, x = 1, is slightly inconsistent with the analytical solution for which the magnetic field was set to zero as $x \to \infty$ but is sufficient to allow verification of the numerical results. The initial condition is, $\vec{B} = \vec{E} = 0$.

Two cases are selected for verification against the analytical solution, $\sigma = 10^{-2}$ *mho/m* and $\sigma = 10^{-4}$ *mho/m*, or $\eta = 1/\left(\mu_0\sigma\right) = 8\times10^7$ m^2/s and $\eta = 8\times10^9$ m^2/s. The time step is selected by setting the von Neumann number, $vnn = \Delta t/\left(\mu_0\sigma\Delta x^2\right)$ = 2.4, yielding time step sizes of $\Delta t = 10^{-12}$ *s* and $\Delta t = 10^{-14}$ *s*, respectively. Comparisons with the 1-D analytical solution are presented in Figs. 13 and 14 where we show the field variation along the centerline of the 2-D domain. The results show very good agreement between the numerical and analytical solutions apart from the anticipated error near the downstream boundary (x = 1), where the two boundary conditions are dissimilar. The solutions also show that the wave diffusion speed is proportional to the electrical diffusivity, η.

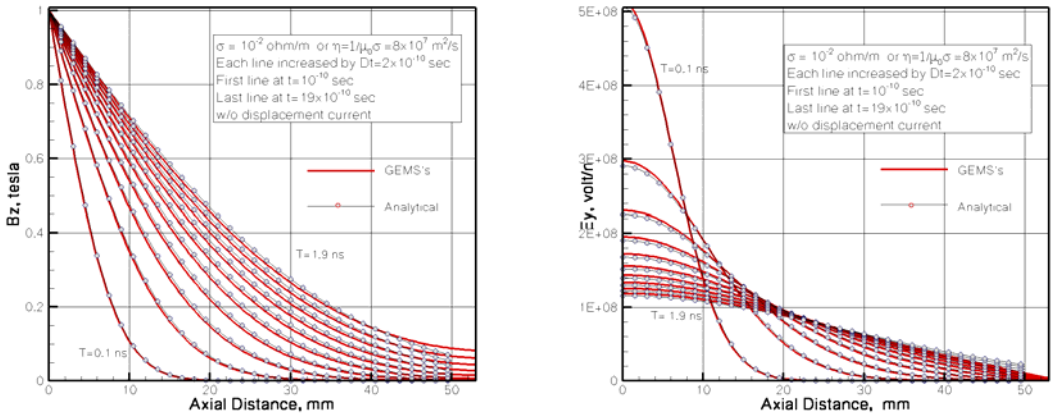

Figure 13. Comparison of GEMS and analytical solution for $\sigma = 10^{-2}$ mho/m (Left: B_z, Right: E_y).

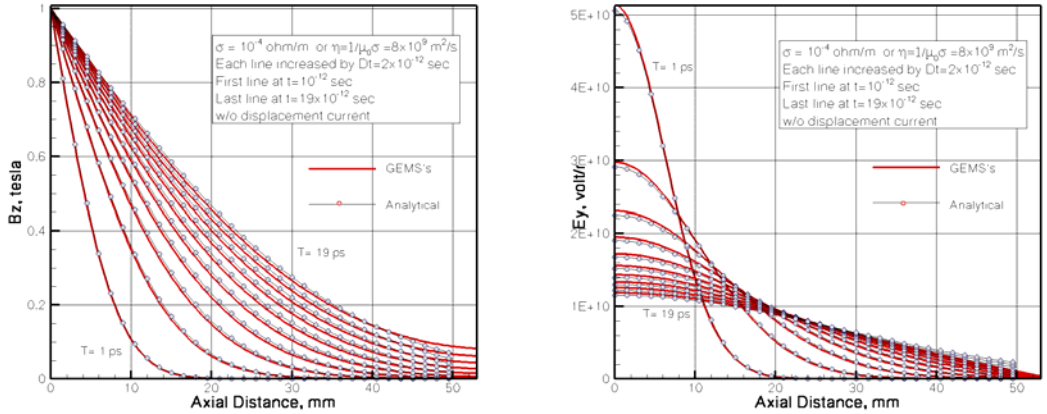

Figure 14. Comparison of GEMS and analytical solution for $\sigma = 10^{-4}$ mho/m (Left: B_z, Right: E_y).

B. Magnetic Diffusion with Finite Displacement Current

We next repeat the $\sigma = 10^{-2}$ *mho/m* calculation with the displacement current term, $(1/c^2)\partial\vec{E}/\partial t$, included. When the displacement current is included, Maxwell's equations for this problem simplify to the telegraph equation whose solution is composed of a precursor lossless wave followed by a residual diffusion wave that is left behind and decays exponentially with time after the initial pulse passes through. Similar characteristics are seen for the $\sigma = 10^{-2}$ *mho/m* calculation in Fig. 15 when displacement current is included. The initial portion of the *B*-field that propagates through the region is composed of a wave front which is immediately followed by a diffusion process. Consequently, the nature of the transient *B*-field is completely different when displacement current effects are included. The diffusion solution from Fig. 14 is shown in blue for reference. The numerical experiments indicate that for the present problem, the displacement current affects the electromagnetic wave when the electrical conductivity of the media falls below approximately 1 *mho/m*. Under such conditions, the MHD assumption of a weakly ionized plasma is not accurate and the full Maxwell equation solver is necessary.

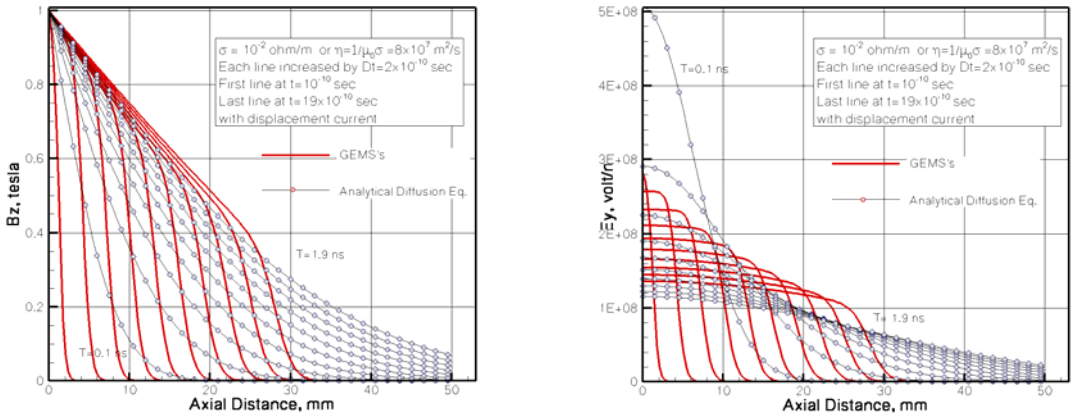

Figure 15. Comparison of numerical field solution with displacement current included (red) with diffusion equation solution (grey) for $\sigma = 10^{-2}$ mho/m (Left: B_z , Right: E_y).

C. Electromagnetic field in two mediums

The next case considers the transient electromagnetic field in an annular vacuum chamber that represents a simplified version of the PPT configuration discussed above. The length, *L*, of the vacuum region is 50 *mm* while the inner and outer walls are formed by concentric, stainless steel cylinders of radius r_1= 22 *mm* and r_2 = 53 *mm* with a wall thickness δ = 3 *mm* as shown in Fig. 16a. In place of the slug of plasma that serves as the propellant, the top of this annular region is enclosed by a stainless steel armature that carries the current from the inner to outer electrode. As noted above, the difficulty in this electromagnetic calculation is that the magnetic field must be carried by wave processes in the vacuum region, whereas in the stainless steel it is carried by diffusion. Hence, the solution of the complete problem requires capability for solving both the diffusion limit and the wave propagation limit simultaneously.

As a first step in addressing this problem we begin by filling the vacuum region with an 'ether' medium of finite conductivity so that both the stainless steel and vacuum regions can be represented by the diffusion approximation. This allows us to again verify that the hyperbolic solution method employed in the GEMS code provides the same

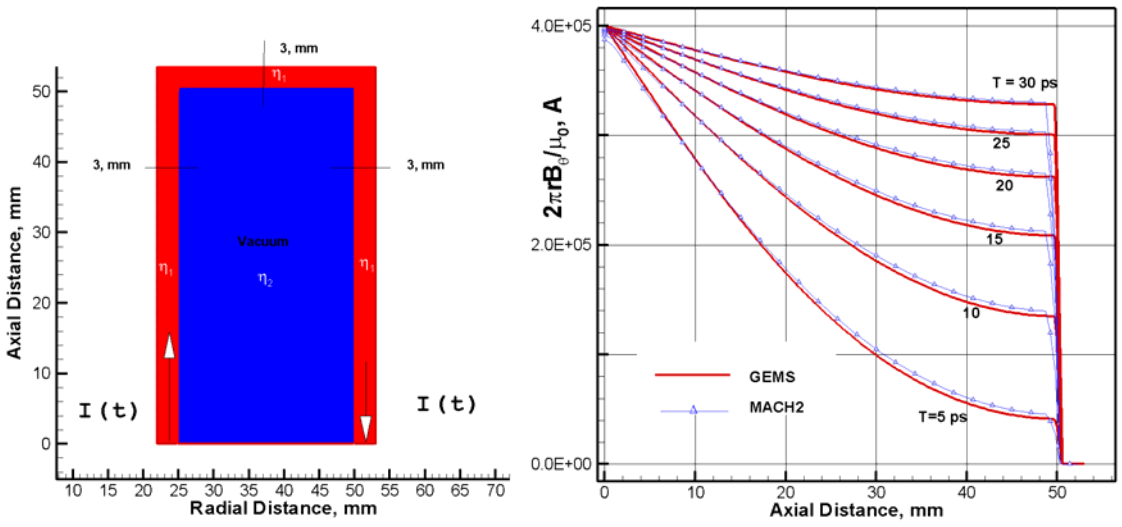

Figure 16. Left: Geometry of concentric stainless steel channels with low conductivity material shown in blue replacing vacuum region in the center and by high conductivity material (stainless steel) shown in red. Right: Comparison of transient magnetic field propagation as computed by GEMS (red) and Mach (blue).

results as the solution of the more traditional magnetic diffusion equation that is obtained from MACH2. Because MACH2 is an MHD code that deals only with the magnetic diffusion equation, it cannot solve the present problem unless the vacuum region has a finite electrical conductivity to propagate magnetic field by diffusion. Following this diffusion calculation, we then include the displacement current effects in GEMS and recompute the solution with the conductivity in the vacuum set identically to zero to contrast the differences in the transient fields when they are propagated by displacement current rather than by physical current.

For the ether solution we set the electrical conductivity in the vacuum region to $\sigma = 10^{-2}$ *mho/m*, and specify the conductivity of the stainless steel walls as $\sigma = 8\text{x}10^{5}$ *mho/m*. The problem is then computed with both MACH2 and GEMS. The time step for the diffusion calculation is set at $\Delta t = 0.1$ *ps* is used to catch the very fast initial wave diffusion phenomena in the vacuum (ether) region. Figure 16b compares the axial distribution of the current flow (the rB_θ field) as a function of axial distance for six different times as predicted by GEMS and MACH2. The field is seen to propagate through the ether in exponential-like fashion. The very high conductivity in the stainless steel wall on the end of the domain as compared to the ether causes the slope of the curves to change discontinuously and to decay very rapidly to zero. On these very short time scales, the current diffuses to only a very thin skin depth in the stainless steel. The close agreement between the GEMS and MACH2 results is further evidence that the wave-like computational scheme in GEMS provides accurate solutions to problems involving pure diffusion.

Contour plots of the rB_θ field for this same case taken from the GEMS solution are presented in Fig. 17 for three time instants. These contour plots indicate that the current flow (the rB_θ field) in the ether is essentially one dimensional with the only two-dimensional effects occurring in the skin effect region inside the stainless steel walls on the sides of the low conductivity region. The grids used in the stainless steel are not sufficiently refined to represent this skin effect accurately, but the plots show that the diffusion depth into the stainless steel is very small. At much longer times (results not shown) the entire current diffuses into the stainless steel and none of the current is carried by the low conductivity 'ether'.

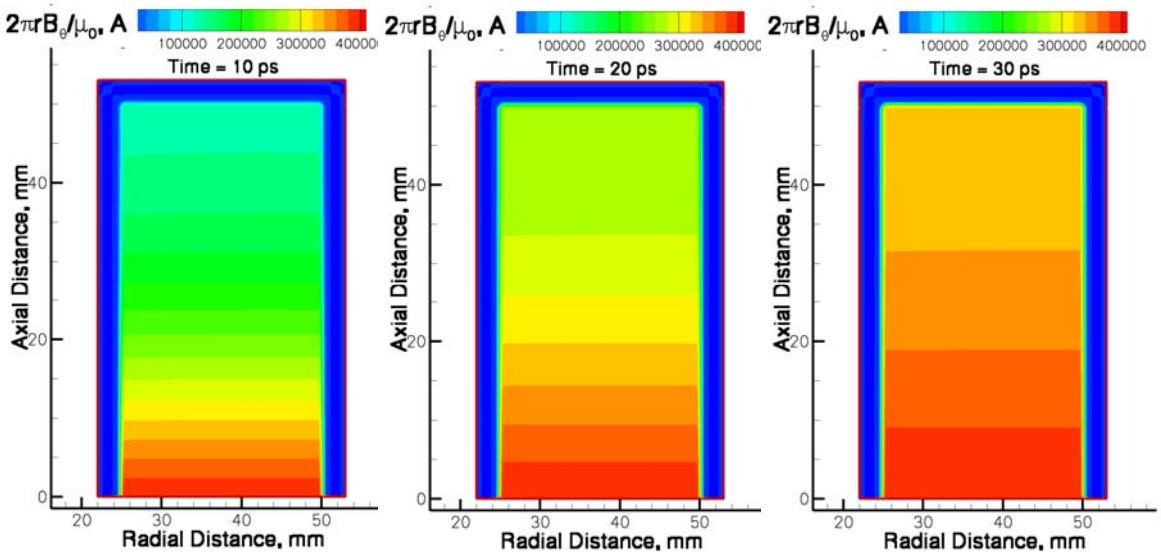

Figure 17. Transient current distribution in 'ether' region surrounded by stainless steel obtained with diffusion equation.

Companion calculations of the same geometry with the displacement current term, $\left(1/c^2\right)\partial\vec{E}/\partial t$, included and the conductivity in the vacuum region set to zero are presented in Figs. 18 and 19. Figure 18 compares the displacement current calculations (full Maxwell solutions) with the diffusion current solution (physical current only, no displacement current) previously shown in Fig. 16. As can be seen, there are significant differences between magnetic field propagation by diffusion and by wave processes. When the conductivity is zero, Maxwell's equations reduce to a pure wave equation and disturbances are carried by a wave moving at the (constant) speed of light. By contrast, the speed of the diffusion wave is proportional to the electrical diffusivity and decreases as the inverse square root of time. Further, the amplitude of the diffusion wave is damped exponentially while the pure

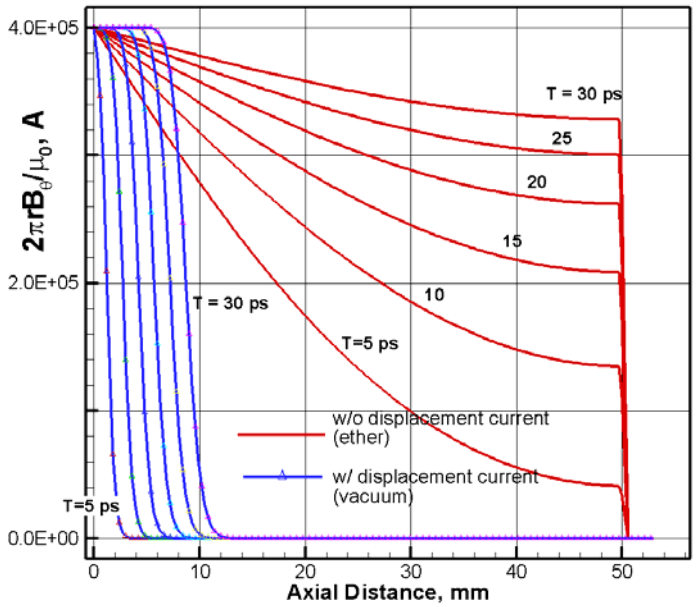

Figure 18. Comparison of displacement current in vacuum with simulated physical current in 'ether' medium.

wave propagating through the lossless medium maintains constant amplitude. For the conductivity value chosen here ($\sigma = 10^{-2}$ *mho/m)*, the diffusion process propagates considerably faster than speed of light and so reaches the end of the domain before the wave solution. (Setting the conductivity to 10^{-2} *mho/m* is arbitrary, and an 'ether' conductivity could be chosen to more closely match the speed of the wave solution, but no attempt to do so has been made here.)The qualitative character of the two families of rB_θ field lines is also different. The field lines are concave downward for the wave solution, while they are concave upward for the diffusion solution, a further reflection that the two physical mechanisms of transport are based upon completely different physics. These numerical results demonstrate the importance of a solution technique that handles all regimes of operation.

Representative contour plots of the rB_θ field at three different times are given in Fig. 19 for the case in which the field is transported by the displacement current. These solutions are at the same times as those in Fig. 17 and give a direct comparison of the impact of the two methods of distributing magnetic field. It is important to note that the parameter, $2\pi rB_\theta / \mu_0$, represents the sum of both the physical current and the displacement current. In Fig. 17 the displacement current is zero (the $\partial \vec{E} / \partial t$ term is omitted) while in Fig. 19 the physical current vanishes in the vacuum region (where the conductivity is zero). The wave solution shown in Fig. 19 does include current along that portion of the electrodes over which the magnetic wave has passed, but is zero in front of it. By contrast the surface current on the stainless steel in the diffusion solutions goes all the way around the closed circuit starting from time

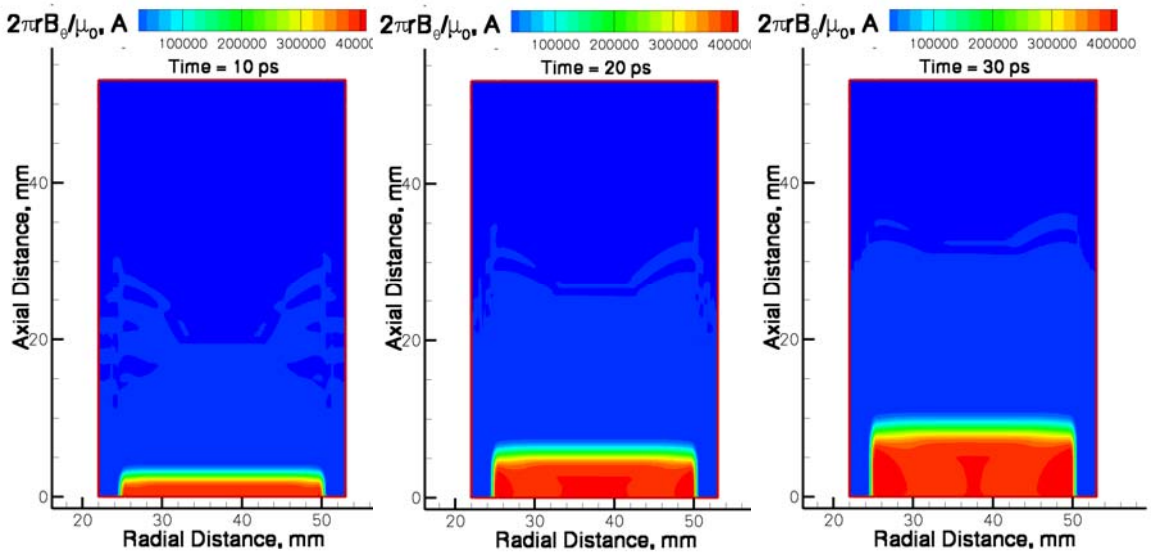

Figure 19. Transient current distribution in vacuum region surrounded by stainless steel as a function of time. Solutions obtained with Maxwell equations including displacement current term.

zero, but with an exponentially small amplitude that increases with time until a final uniform current is established.

The above diffusion and Maxwell solutions show major differences on a picosecond time scale, but the many of the key physics in PPA simulations occur on a microsecond time scale. It is important to ascertain whether any of these early time differences remain at later times or whether additional displacement current effects are introduced during the PPA cycle. Specific answers to these questions require detailed simulations of the entire pulse phenomena and careful comparisons with the companion experiments, but to give a first indication of differences at longer times, we here present some longer time simulations of the displacement current case for the present simplified problem. Clearly, at infinite time, both the wave solution and the diffusion solution will approach the same steady state condition with uniform magnetic field and zero current in the vacuum region and a linear magnetic field and uniform current density in the stainless steel. (The steady state diffusion solution will have a minute current in the vacuum region determined by the ratios of the conductivities in the stainless steel and ether.) The results in Figs. 16 and 17 can easily be extrapolated to steady conditions, whereas the wave solutions in Figs. 18 and 19 are so early in time that the approach to steady state cannot be anticipated. To address this issue, we present some longer time solutions in Fig. 20 and 21.

Figure 20 shows $2\pi r B_\theta / \mu_0$ profiles at various times in a fashion identical to that used in Fig. 18, but for time increments of 100 *ps*, starting from 100 *ps* and going to 1 *ns*. Looking first at Profiles 1 and 2, the shapes are similar to those previously shown in Fig. 18. When the wave reaches the higher conductivity material it reflects with approximately double the amplitude and then propagates back toward the boundary where the magnetic field was originally imposed (Profiles 3 and 4) where it again reflects and repeats the process (Profiles 5 through 10). Each succeeding reflection from the stainless steel transmits a small fraction of the energy into the stainless steel where diffusive effects dominate. This transmission of the magnetic field into the stainless steel results in a gradual amplitude decay in the vacuum region. The diffusion into the higher conductivity material can also be seen on the right side of the figure. This diffusion rate has been amplified by decreasing the conductivity in the stainless steel to 800 *mho/m* for this calculation.

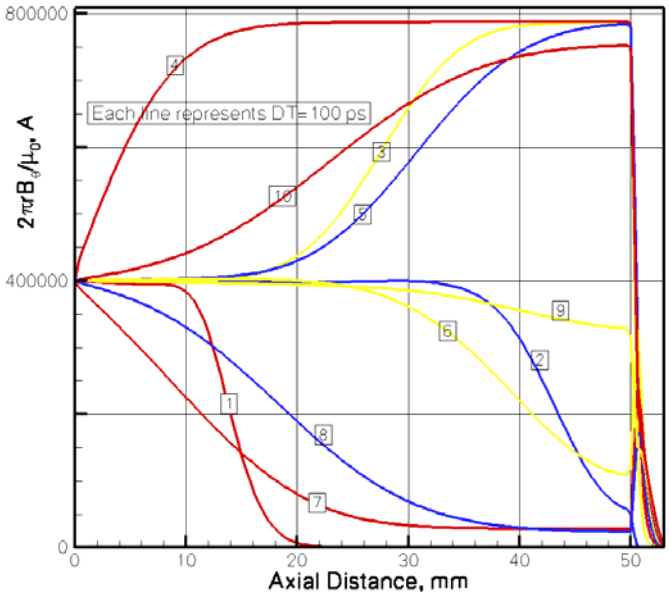

Figure 20. Axial profiles of $2\pi r B_\theta / \mu_0$ along centerline of vacuum and regions for various times from 100 to 1000 ps. Stainless steel conductivity changed to 800 mhos/m.

Figure 21 shows the time history of the magnetic field intensity ($2\pi r B_\theta / \mu_0$) at Point *A* in the inset as a function of time for the diffusion solution (Fig. 16) and the wave equation solution (Figs. 18 and 20). For the diffusion calculation the vacuum region has been filled with ether ($\sigma = 10^{-2} mho/m$) and the displacement current is set to zero. For the wave solution, the conductivity in the vacuum is zero (σ =0) and displacement current is the only mechanism for propagating the magnetic field through the vacuum. For the case without displacement current, the magnetic field at Point *A* is seen to increase monotonically from zero to the imposed maximum in approximately 100 *ps*. The rate of increase is, of course, determined by the conductivity level in the ether. The wave solution, however, behaves much differently and approaches the steady solution through a damped oscillatory trajectory. As noted above, the damping rate is determined by the conductivity of the adjacent material. The present solution, which is based upon the same *800 mhos/m* conductivity used for Fig. 20, approaches steady state conditions at about 20 *ns*. An analogous calculation with the conductor set at 8 *mhos/m* showed much more rapid damping and reached steady conditions at approximately 0.3 *ns*, whereas computational attempts at $\sigma = 8 \times 10^5 mho/m$ decayed exceedingly slowly (in line with an expected decay in 3 μs). The plasma armature in the PPA would be expected to have conductivities much lower than stainless steel, and the imposed magnetic field would vary with time rather than be constant, but the present results provide some understanding of the manner in which wave-transported fields differ from diffusion-transported fields.

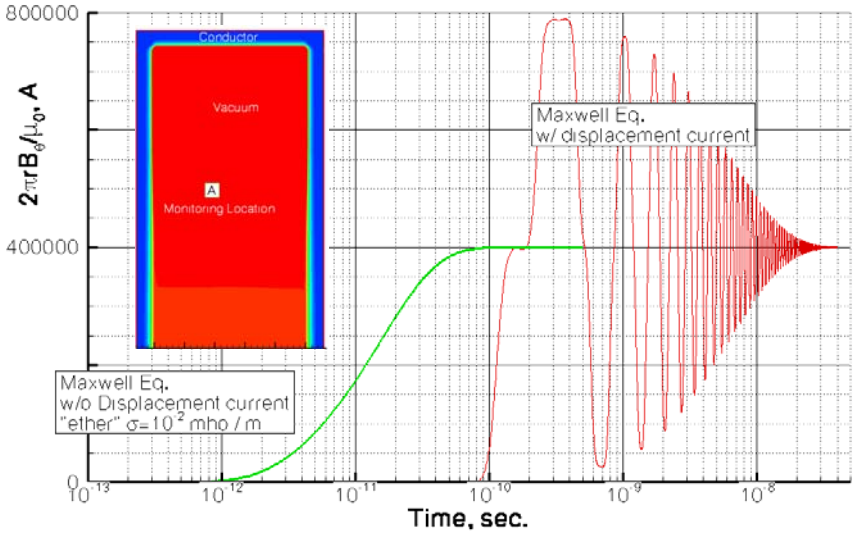

Figure 21. Time history of Maxwell equation solutions with and without displacement current. Results correspond to magnetic field at Point *A* in inset.

V. Summary and Conclusions

A laboratory prototype pulsed plasma accelerator that has been designed for accurate diagnostics rather than thruster performance to provide data with which our computer simulations can be compared has been described. The thruster has been successfully fired and the collection of photographic images, laser interferometer data, Rogowski coil data, and B-dot probe data is ongoing. These measurements will provide data with which MACH2 and GEMS simulations can be compared.

Preliminary MACH2 simulations of the thruster have demonstrated the need for a full Maxwell equation solver such as the GEMS code that can accurately model wave propagation as well as propagation by diffusion in devices that have regions of dense plasma next to regions of near vacuum. To demonstrate the capability of the GEMS code for the full Maxwell equations, we utilized numerical experiments where the Maxwell solver is applied in three different situations. The first case included the diffusion of a magnetic field through a finite conductor in response to a step change in the magnetic field at the boundary. Comparisons between the GEMS and analytical solutions indicate very good agreement and also show that the wave diffusion speed is proportional to the electrical diffusivity.

The second case involved comparisons of the approximate diffusion solution to a complete Maxwell solution for cases where the diffusivity is small enough that wave processes becomes important. Results of this case indicate that the displacement current affects the electromagnetic wave when the electrical conductivity of the medium falls below approximately 1 *mho/m*. Under such conditions, the MHD assumption of a weakly ionized plasma is not accurate and the full Maxwell equation solver is necessary.

The final test case was one in which the magnetic field is propagated through a domain composed of a vacuum region enclosed by finite conducting walls. For this last case, GEMS solutions were compared with MACH2 solutions, and the results show excellent agreement between the present code and the MACH2 code, while also showing the dramatic differences in the manner in which magnetic fields propagate by wave processes sustained by displacement current, and in diffusion processes sustained by physical current. Future comparisons of experimental measurements from the laboratory prototype pulsed plasma accelerator and simulations from both GEMS and MACH2 are planned for the near future.

Acknowledgments

This work was partially supported by the Arnold Engineering and Development Center under contract #F40600-00-D-001 0024. The authors would like to thank the Propulsion Research Center at Marshall Spaceflight Center for

the loan of the high voltage capacitors used in the experimental phase of this work.

References

[1]Moeller, T., Keefer, D., and Rhodes, R., "Experimental Pulsed Plasma Thruster for Code Evaluation," The 31st IEEE International Conference on Plasma Science, Baltimore, MD, June 28 – July 1, 2004.

[2]Smith, L. M., Keefer, D. R., and Wright, N. W., "A fiber-optic interferometer for *in situ* measurements of plasma number density in pulsed-power applications," *Review of Scientific Instruments*, Vol. 74, No. 7, July 2003, pp. 3324-3328.

[3]Peterkin, R. E., Frese, M. H., and Sovenec, C. R., "Transport of magnetic flux in an arbitrary coordinate code," *J. Computat. Phys.*, Vol. 140, 1998, pp. 148-171.

[4]Rashleigh, S. C., and Marshall, R. A, "Electromagnetic acceleration of macroparticles to high velocities," *Journal of Applied Physics*, Vol. 49, No. 4, April 1978, pp. 2540-2542.

[5]Sutton, G. W., and Sherman, A., "Engineering Magnetohydrodynamics," McGraw-Hill, New York, 1965.

[6]Bouillard, J. X., Krazinski, J. L., Vanka, S. P., and Berry, G. F., "Performance of a Multigrid Three Dimensional MHD Generator Calculation Procedure," 27th Symposium Engineering Aspects of Magmetohyrodynamics, June 27-29, 1989, Reno, Nevada, pp. 5.2.1-5.2.12.

[7]Powell, K. G., Roe, P. L., Myong, Rho Shin, Gombosi, Tamas and De Zeeuw, D. L., "An Upwind Scheme for Magnetohydrodynamics," 12th AIAA CFD Meeting, AIAA Paper 95-1704-CP, June 1995, pp. 661-672

[8]Choueiri, E. Y., "Anomalous Resistivity and Heating in Current-Driven Plasma Thrusters," Physics of Plasmas, Vol. 6, No. 5, 1999, pp 2290-2306

[9]K. Sankaran, E. Y. Choueiri, and S. C. Jardin, "Comparison of Simulated Magnetoplasmadynamic Thruster Flowfields to Experimental Measurements," AIAA Journal of Propulsion and Power, Vol. 21, No. 1, pp 129-138, 2005.

[10]Li,D., Keefer, D., Rhodes, R., and Merkle, C. L., and Thibodeaux,R., "Analysis of MHD Generator Power Generation," AIAA Journal of Propulsion and Power, Vol. 21, No. 3, pp424-432, 2005.

[11]Munz, C. D., Ommes, P. and Schneider, R., "A Three-dimensional Finite-Volume Solver for the Maxwell Equations with Divergence Cleaning on Unstructured Meshes," Computational Physics Communications, 130, pp 83-117, 2000

[8]Li D., Xia G.and Merkle C.L, "Large-Scale Multidisciplinary Computational Physics Simulations using Parallel Multi-physics Zone Methods," The International Conference on Parallel Computational Fluid Dynamics, University of Maryland, College Park Campus, May 24-27, 2005

[12]Li, D., Venkateswaran, S., Lindau, J. and Merkle, C. L.,A Unified Computational Formulation for multi-Component and Multi-Phase Flows, 43rd AIAA Aerospace Sciences Meeting and Exhibit, January 10-13, 2005, Reno, NV, AIAA 2005-24906.

[13]Li, D., Xia,G.P., Venkateswaran, S. and Merkle, C., "Computational Framework for Complex Fluid Physics Applications," Third International Conference on Computational Fluid Dynamics, Canada 2004

[14]Niewood, E. H., "An Explanation for Anode Voltage Drops in an MPD," PhD thesis, MIT,

[15]Frese, M., "MACH2: A Two-Dimensional Magnetohydrodynamic Simulation Code for Complex Experimental Configurations," Mission Research Corporation, Technical Report AMRCP-814, September 1987.